



Mapping of heavy metal pollution in stream sediments using combined geochemistry, field spectroscopy, and hyperspectral remote sensing: A case study of the Rodalquilar mining area, SE Spain

Eunyoung Choe^a, Freek van der Meer^{b,c,*}, Frank van Ruitenbeek^b, Harald van der Werff^b, Boudewijn de Smeth^b, Kyoung-Woong Kim^a

^a Gwangju Institute of Science and Technology (GIST), Department of Environmental Science and Engineering, 1 Oryong-dong, Buk-gu, 500-712 Gwangju, Republic of Korea

^b International Institute for Geo-information Science and Earth Observation (ITC), Department of Earth Systems Analysis, Hengelosestraat 99, 7500 AA Enschede, The Netherlands

^c Utrecht University, Department of Physical Geography, Heidelberglaan 2, 3508 TA Utrecht, The Netherlands

ARTICLE INFO

Article history:

Received 5 September 2007

Received in revised form 26 March 2008

Accepted 29 March 2008

Keywords:

Geochemical

Heavy metal

HyMAP

Hyperspectral

Mapping

Spectral parameter

Spectroscopy

Statistical

Stream sediment

ABSTRACT

The aim of this study is to derive parameters from spectral variations associated with heavy metals in soil and to explore the possibility of extending the use of these parameters to hyperspectral images and to map the distribution of areas affected by heavy metals on HyMAP data. Variations in the spectral absorption features of lattice OH and oxygen on the mineral surface due to the combination of different heavy metals were linked to actual concentrations of heavy metals. The ratio of 610 to 500 nm ($R_{610,500 \text{ nm}}$) in the visible and near-infrared (VNIR) range, absorption area at 2200 nm ($\text{Area}_{2200 \text{ nm}}$), and asymmetry of the absorption feature at 2200 nm ($\text{Asym}_{2200 \text{ nm}}$) showed significant correlations with concentrations of Pb, Zn, and As, respectively. The resulting spectral gradient maps showed similar spatial patterns to geochemical gradient maps. The ground-derived spectral parameters showed a reliable quantitative relationship with heavy metal levels based on multiple linear regression. To examine the feasibility to applying these parameters to a HyMAP image, image-derived spectral parameters were compared with ground-derived parameters in terms of R^2 , one-way ANOVA, and spatial patterns in the gradient map. The $R_{1344,778 \text{ nm}}$ and $\text{Area}_{2200 \text{ nm}}$ parameters showed a weak relationship between the two datasets ($R^2 > 0.5$), and populations of spectral parameter values, $\text{Depth}_{500 \text{ nm}}$, $R_{1344,778 \text{ nm}}$, and $\text{Area}_{2200 \text{ nm}}$ derived from the image pixels were comparable with those of ground-derived spectral parameters along a section of the stream channel. The pixels classified in the rule image of $\text{Depth}_{500 \text{ nm}}$, $R_{1344,778 \text{ nm}}$, and $\text{Area}_{2200 \text{ nm}}$ derived from a HyMAP image showed similar spatial patterns to the gradient maps of ground-derived spectral parameters. The results indicate the potential applicability of the parameters derived from spectral absorption features in screening and mapping the distribution of heavy metals. Correcting for differences in spectral and spatial resolution between ground and image spectra should be considered for quantitative mapping and the retrieval of heavy metal concentrations from HyMAP images.

© 2008 Elsevier Inc. All rights reserved.

1. Introduction

The distribution and diffusion of heavy metals throughout mining areas are an important issue because abandoned tailings¹ can be a major source of environmental pollution. A general method for surveying the spatial distribution of heavy metals involves the

systematic sampling and laboratory analysis of stream sediment samples followed by interpolation of the point results in compiling distribution maps (Ferrier, 1999; Kemper & Sommer, 2002); however, such an approach is time-consuming and costly. Remote sensing has been used in investigations of the dispersion of heavy metals as a rapid method of preliminary analysis, and the use of high-quality imaging spectrometer (hyperspectral) data may improve upon previous results. Several studies have indicated the possibility of applying field and imaging spectroscopy in the identification of minerals containing heavy metals as an indicator of contamination in mining areas (Farrand & Harsanyi, 1997; Ferrier, 1999). Montero et al. (2005) assessed the potential of abandoned mines for acid mine drainage (AMD) by characterizing waste rock associated with acid drainage, and Sares et al. (2004) indirectly determined the pH of an

* Corresponding author. International Institute for Geo-information Science and Earth Observation (ITC), Department of Earth Systems Analysis, Hengelosestraat 99, 7500 AA Enschede, The Netherlands. Tel.: +31 53 4874353; fax: +31 53 4874336.

E-mail address: vdmeer@itc.nl (F. van der Meer).

¹ Tailings, the materials left over after mining activities (i.e., the extraction of ore from the host mineral).

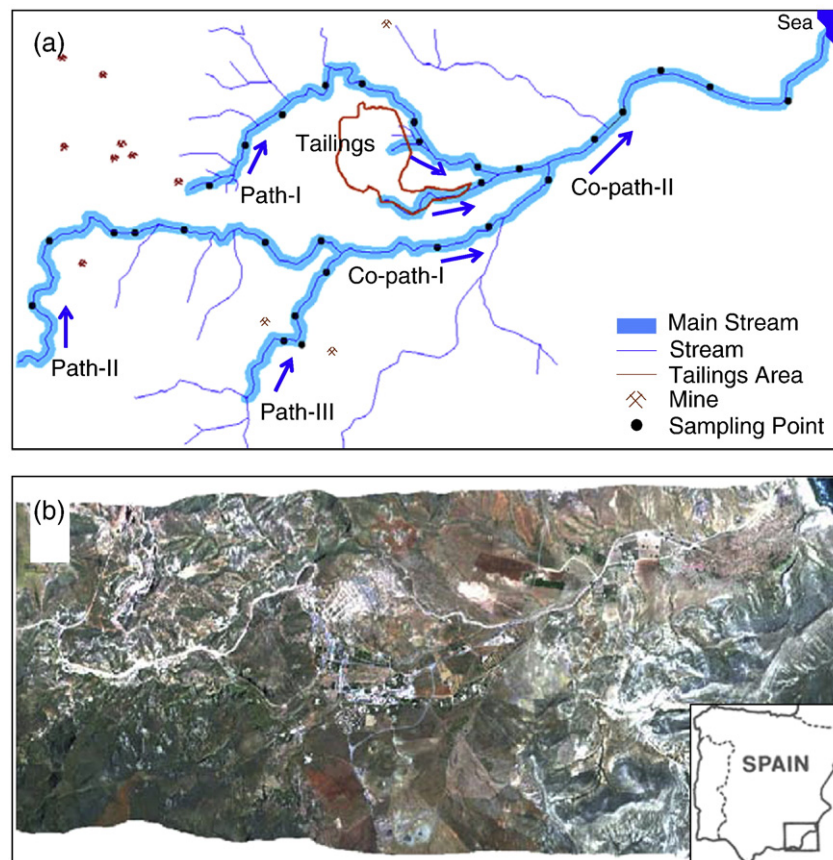


Fig. 1. Location map and HyMAP image of the Rodalquilar area, SE Spain. (a) Locations of sampling points along the studied main stream, showing the five sections. (b) HyMAP image acquired in 2004.

AMD-affected stream by identifying iron-bearing minerals precipitated on the streambed. In terms of assessing the heavy metal level in soils, Wu et al. (2005) and Kemper and Sommer (2002) estimated metal concentrations using reflectance spectroscopy and statistical prediction models; the authors suggested the possibility of applying their technique to remote sensing.

In the present study, it is assumed that although heavy metals are spectrally featureless in the visible and near-infrared parts of the electromagnetic spectrum, the spectral signatures of minerals that bind heavy metals can be used for the indirect detection and mapping of metal dispersion using spectrometer data. This study focuses on deriving parameters from spectral responses associated with heavy metals in soil as a fingerprint to be used in tracing the metals. We also explore the possibility of extending ground-derived spectral parameters to images, and the mapping of areas affected by heavy metals on HyMAP data using the spectral parameters themselves as an initial step in the retrieval and quantitative mapping of heavy metals from hyperspectral images. These aims are achieved by characterizing the spectral variation of minerals that bind heavy metals, based on the theory of metal sorption mechanisms in soil. Clay and metal oxide minerals are considered because heavy metals are easily adsorbed onto these minerals in soils. These mineral surfaces in soil have functional groups capable of forming complexes with inorganic and organic ions. In particular, inorganic hydroxyl groups that combine with surface Al, Fe, Mn, or Si on metal oxides or the edges of clay minerals are one of the major surface functional groups (Zachara & Westall, 1999). Inorganic hydroxyl groups are not only a major adsorption site, but also act as chromophores² in mineral components.

² Chromophore, a parameter or substance (chemical or physical) that significantly affects the spectral shape and nature of materials (Ben-Dor et al., 1999).

2. Background

2.1. Binding mechanism of heavy metals onto minerals

To explain possible variations in spectral signal due to heavy metals bound onto minerals, it is necessary to consider the metal binding reaction onto the mineral surface. This approach starts from the possibility that the spectral assignment position of minerals can change with chemical composition and surface activity (Ben-Dor et al., 1999). Despite the occurrence of otherwise similar minerals in different samples, variations in spectral features (e.g., shifts in the peak wavelength) may occur depending on the nature of highly enriched cations in the mineral.

The surface complexation model of the binding reactions of heavy metals describes the binding of metal ions to the surface functional group on the mineral surface to form a more stable molecular unit (Christl & Kretzschmar, 1999; Zachara & Westall, 1999). Inorganic hydroxyl groups that bind to surface Al, Fe, Mn, or Si on oxides or Al and Si exposed on the edges of clay minerals are the main surface functional groups (Sparks, 1995; Zachara & Westall, 1999). The surface complexation model is based on the fact that the sorption of ions takes place at specific surface sites (Dzombak & Morel, 1990; Christl & Kretzschmar, 1999). Sites that originate from a broken mineral lattice, known as variable charge sites, are relatively stable over long time scales (Roberts et al., 2005). Metal cations (M^{2+}) adsorbed onto such hydroxylated surface sites (ROH, in which R can be Al, Fe, Mn, Si, etc. upon mineral surfaces) are generally described as follows:



In this reaction, H^+ ions are released from ROH (e.g., AlOH, SiOH, or FeOH) on the mineral surface, such as clay and metal oxides, as M^{2+}

cations are adsorbed; consequently, an increase in the amount of metal cations results in a decrease in the extent of the hydroxyl surface site (i.e., ROH) and an increase in RO at the mineral surface. As a consequence of the binding reaction of heavy metals, decreasing ROH and increasing RO (e.g., FeO) on the surfaces of clay and oxide minerals may result in variations in the shapes of their absorption peaks (e.g., depth, area, or asymmetry of reflectance spectra) at around 2200 nm and 500–1000 nm, respectively, once heavy metals are bound to the minerals.

3. Description of the study area

The study site is the Rodalquilar gold-mining area in SE Spain (Fig. 1), part of the Cabo de Gata volcanic field. The rocks in this area are dominated by quartz, alunite, jarosite, pyrophyllite, illite, kaolinite, hematite, and related minerals. Gold mineralization at Rodalquilar resulted from a hydrothermal alteration system that produced high levels of sulfidation (Arribas et al., 1989; Rytuba et al., 1990).

Small-scale mining of silver-rich galena from veins took place for many centuries; however, from the 1940s to the 1960s, gold mining was undertaken at a larger scale, including both underground mining and open pits. Mining was concentrated along the east wall of the Cinto caldera, approximately 1.5 km northwest of Rodalquilar. In this area, gold occurs in association with pyrite that also contains high levels of arsenic and other metals. High levels of pollutants derived from waste rock, tailings, and material associated with leaching operations have been reported from stream sediments along the entire length of the rambla to the coast (Wray, 1998; Ferrier, 1999; Moreno et al., 2007).

4. Materials and methods

To observe the relationship between heavy metal levels and spectral responses, spectral variation with changing concentrations of heavy metals was defined as the parameters derived from spectral absorption features such as peak depth, area, asymmetry, and band ratio. These parameters were linked to heavy metal concentrations via correlations between them. Based on the obtained statistical relationships, we compared gradient maps of heavy metal levels and spectral parameter values. In terms of quantitative relationships, the spectral parameters were used for a linear regression with measured concentrations. The image-derived spectral parameters were compared with ground-derived spectral parameters for individual sampling points, and applied to image classification for mapping the distribution of heavy metals in the area adjacent to the streamline. The obtained results were then compared with a distribution map compiled from the ground dataset.

4.1. Ground dataset

4.1.1. Experimental data

The 49 samples of dry sediments were collected from stream channels in the Rodalquilar area that drain from the Au and Pb–Ag mining areas and mill tailings. The 20 samples collected from branch streams were excluded from spatial analysis such as mapping and image processing because spatial patterns were only considered along the main streamlines. Samples were sieved in the field to obtain the soil fraction smaller than 2 mm. The sampled drainage pattern was divided into five main sections: path-I, path-II, and path-III, representing the upper reaches of the sampled stream, and co-path-I and co-path-II, which lie below the confluences of these upper parts. This division enabled observations of the distribution of heavy metal concentrations (see Fig. 1(a)). For chemical analysis, sediment samples were preprocessed by total extraction, carried out by adding aqua regia (3:1 ratio of HCl to HNO₃) for decomposition of the greater part of any heavy metals present in soils. The concentrations of a large

number of heavy metals were analyzed using inductively coupled plasma-atomic emission spectrometry (ICP-AES) and atomic-absorption spectroscopy (AAS); among these metals, As, Cu, Pb, and Zn were considered to be indicative of environmental pollution.

In terms of spectral measurements, stream sediment samples were measured in the laboratory using an ASD FieldSpec Pro (Analytical Spectral Devices Inc.) equipped with a contact probe, using a Spectralon Diffuse Reflectance Panel for reflectance calibration. The

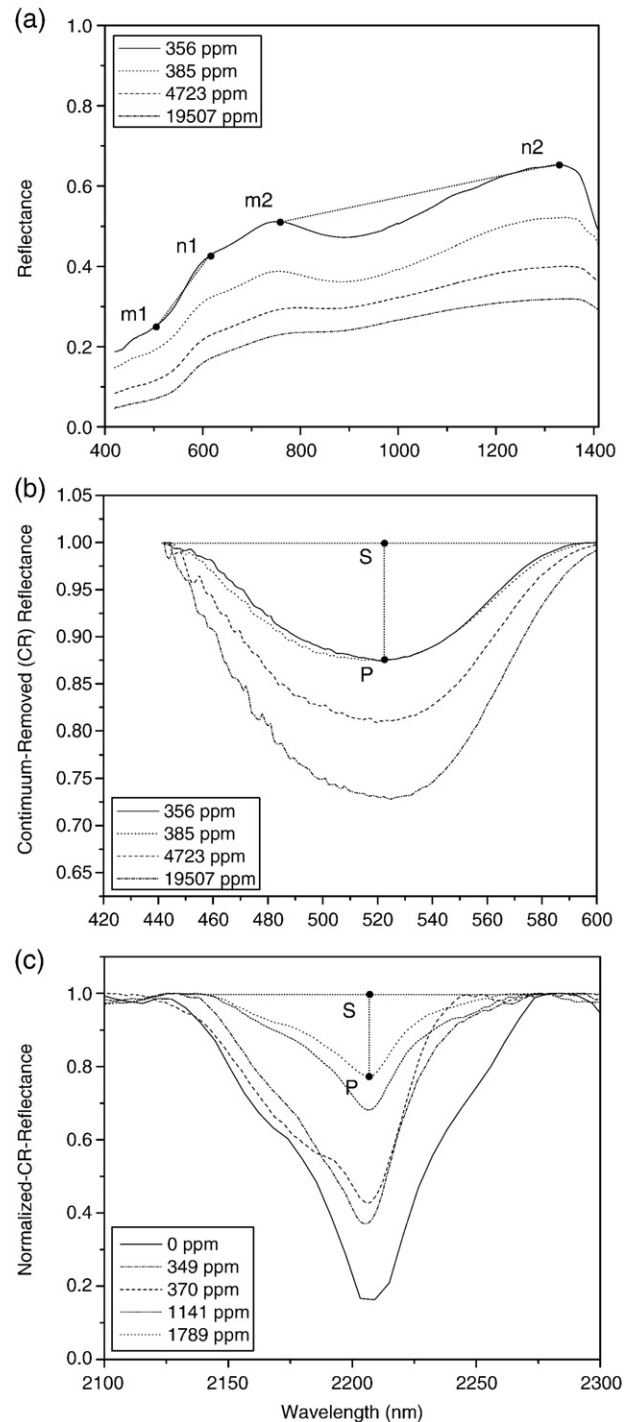


Fig. 2. Spectral variations in the VNIR and SWIR ranges related to lattice OH and oxygen binding with heavy metals as a function of heavy metal concentrations. (a) Ratio 610,500 (n_1 , m_1) and ratio 1344,778 (n_2 , m_2) in the VNIR range. (b) Absorption depth (S, P) at about 500 nm for field samples with heavy metal concentrations ranging from 356 to 19507 ppm. (c) Absorption depth (S, P) at about 2200 nm for sediment samples with heavy metal concentrations ranging from 349 to 1789 ppm.

instrument covers the 350–2500 nm range, using the VNIR (350–1050 nm), SWIR1 (1000–1800 nm), and SWIR2 detectors (1800–2500 nm). Samples were contained in a 60 × 15 mm dish with a sample depth of approximately 8 mm and spectrally measured using the contact probe, which involves surface-to-surface contact measurements with a spot size of 10 mm and a light source (i.e., halogen bulb). The internal light source illuminated the sample surface, and all spectral measurements were carried out in a dark room to avoid interference by stray light.

4.1.2. Derivation of spectral parameters

Based on metal binding mechanisms, variations in absorption features such as the peak depth and peak area of the hydroxyl lattice on clay or oxide minerals were observed at around 2200 nm (Fig. 2), at which point occurs the OH absorption feature of $\nu_{\text{OH}} + \delta_{\text{OH}}$ in combination mode (Ben-Dor et al., 1999). Molecules that combine with Fe have absorption features that lie mainly in the VNIR region because of the crystal field and the charge transfer effect (Gaffey et al., 1993; Ben-Dor et al., 1999), thereby giving rise to Fe–O absorption features in the 400–1200 nm range.

Obtained spectra were continuum-removed and normalized to enhance the spectral absorption features. The continuum-removal analysis proposed by Clark and Roush (1984) is the standard transformation in spectroscopy (van der Meer, 2006). In this approach, the continuum that is a convex hull of straight-line segments is fitted over a reflectance spectrum and subsequently removed by division or ratioing relative to the complete reflectance spectrum (van der Meer, 2006).

Variations in the spectral absorption features of functional groups that bind heavy metals were measured separately in the VNIR and SWIR regions to derive spectral parameters. The spectral features in the VNIR region are known to be associated with iron, e.g., Fe–O (Ben-Dor et al., 1999). In this range, the shape of the absorption peak was measured from the continuum-removed spectra, and the wavelength band ratio was calculated from the reflectance spectra without continuum-removal (see Fig. 2). Variations in absorption features around 2200 nm associated with ROH (R: Al, Si, Fe, Mn, etc.) on the surface of clay or metal oxide minerals were measured from normalized continuum-removed spectra.

4.1.3. Statistical processing

The relationships between the spectral absorption feature parameters and heavy metal concentrations were assessed using the Pearson correlation coefficient. The bivariate correlation was produced at a 95% confidence level (2-tailed).

Table 1

Heavy metal concentrations within stream sediment samples collected from the five analyzed pathways

Stream Section	Statistics	Heavy metal concentration (mg/kg: ppm)			
		Cu	Pb	Zn	As
Total	Mean	129.7	1412.7	200.9	292.2
	Highest	584.5	18,811.3	728.1	826.9
	Lowest	46.3	96.0	61.3	62.3
Path-I	Mean	92.2	336.4	148.5	353.3
	Highest	143.9	1024.6	274.4	826.9
	Lowest	60.7	110.8	61.3	112.0
Path-II and co-path-I	Mean	118.7	410.6	193.8	127.8
	Highest	275.6	1187.2	472.5	194.3
	Lowest	46.3	96.0	65.4	62.3
Path-III	Mean	328.2	8038.5	469.8	238.4
	Highest	584.5	18,811.3	728.1	375.5
	Lowest	49.1	277.0	115.7	157.7
Co-path-II	Mean	68.1	268.6	104.7	541.7
	Highest	101.8	371.9	124.3	675.4
	Lowest	50.2	167.1	88.2	414.0

Table 2

ERL and ERM guideline values for trace metals (ppm, dry wt.)

Element	Guidelines	
	ERL ^a	ERM ^b
As	8.2	70
Cu	34.0	270
Pb	46.7	218
Zn	150.0	410

^a Effects range-low.

^b Effects range-median.

To observe the quantitative relationship between spectral parameter values and metal levels, two kinds of multiple linear regression, with stepwise and enter methods, were applied. For the stepwise multiple linear regression, at each step the independent variable not in the equation and with the smallest probability of F is entered, provided that the probability is sufficiently small. Variables in the regression equation are removed if their probability of F becomes sufficiently large. The method terminates when no more variables are eligible for inclusion or removal. For enter multiple linear regression, a procedure for variable selection is adopted in which all variables in a block are entered in a single step (Hartman, 2000).

4.1.4. Mapping of the ground dataset

To compare the spatial pattern of elements in the distribution maps of heavy metal levels with that in the maps associated with spectral parameter values, gradient maps for each dataset were compiled within a 40-m-wide bufferzone³ from the streamline. Kriging interpolation was used as the gridding method in producing the gradient maps. This method produces visually appealing maps (e.g., gradient maps) from irregularly spaced data and expresses the spatial trends in each dataset. As described above, the streams were divided into five sections to facilitate the description of the spatial patterns observed in the gradient maps.

4.2. Image dataset

4.2.1. HyMAP image

The image data used in this study was acquired in 2004 during the HyEUROPE 2004 campaign using the airborne imaging spectrometer HyMAP operated by HyVista Corporation (Fig. 1(b)). The sensors collected reflected solar radiation in 126 narrow bands over the 450–2500 nm wavelength range and with continuous spectral coverage except for the 1400 and 1900 nm atmospheric water bands (Cocks et al., 1998). The spatial configuration of the instrument yielded a spatial resolution of 4 m. The HyMAP data were atmospherically corrected using the ATCOR 4 model.

4.2.2. Degree of spectral similarity between HyMAP image and field spectrometer data

To assess the degree of similarity between the reflectance spectra of HyMAP images and ground-measured spectra, the values of image pixels corresponding to the locations of ground sampling points along the main stream channels were compared with ground spectrometer data. The degree of spectral similarity between image pixels and ground spectra was measured to evaluate the possibility of applying the spectral processing of ground data to the image. We measured the degree of spectral similarity of pixels on a classified image that correspond to the GPS coordinates of each field sampling point and the eight surrounding pixels; the most reliable pixel of the nine was then selected, taking into account geocoding errors of the image and GPS data. The degree of spectral similarity was measured using spectral angle mapper (SAM), which determines the degree of spectral

³ Bufferzone, a border area that acts as a barrier separating or surrounding an area designated for special protection.

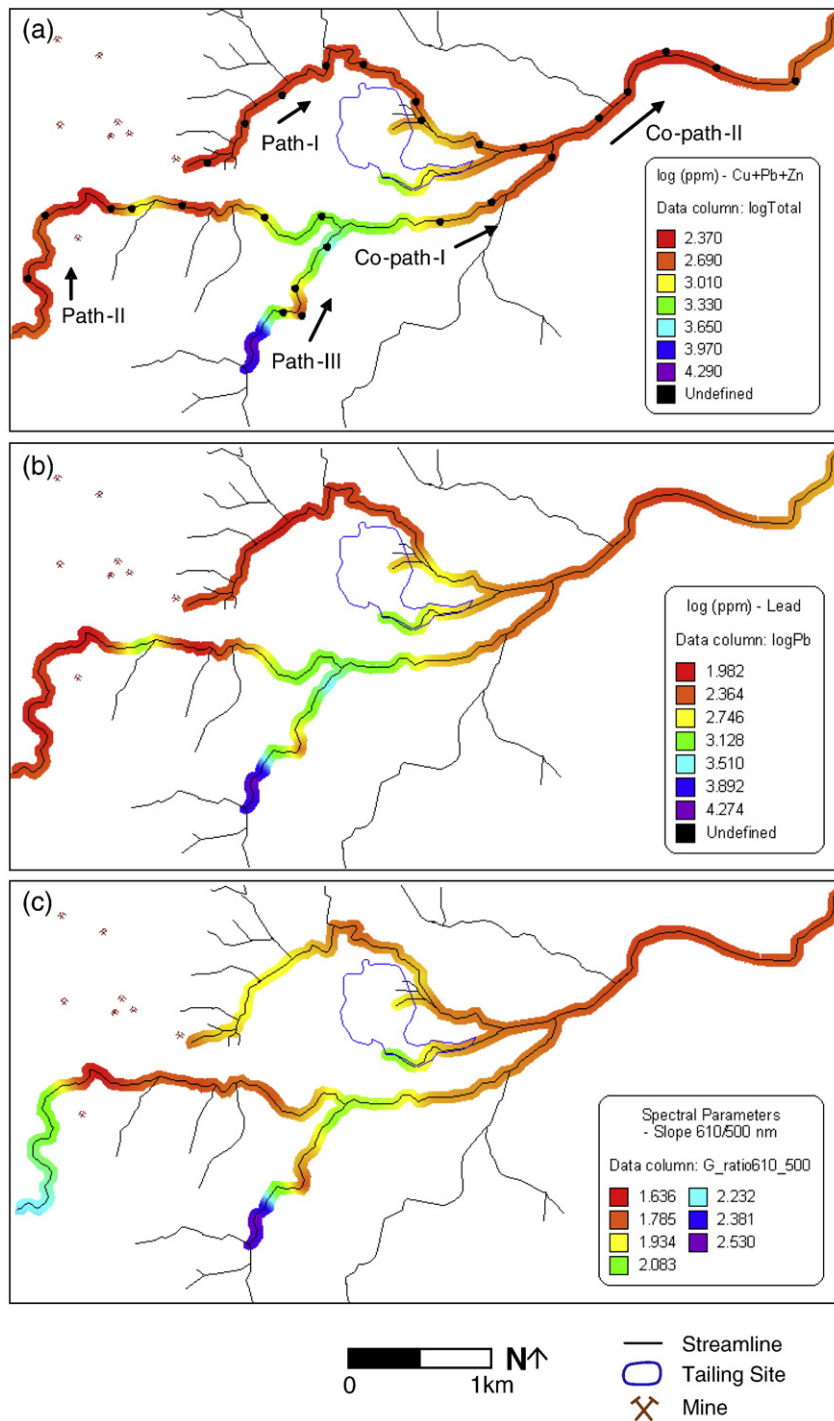


Fig. 3. Comparison of spatial patterns in gradient maps for (a) total concentration, (b) Pb concentration, and (c) $R_{610,500 \text{ nm}}$.

similarity between two spectra by calculating the angle $\theta(\vec{x})$, treating the spectra as vectors in a space with dimensionality equal to the number of bands (Kruse et al., 1993). The spectral angle, $\theta(\vec{x})$, for images I and $\vec{x} \in I$, is given by

$$\theta(\vec{x}) = \cos^{-1} \left(\frac{f(\lambda) \cdot e(\lambda)}{\|f(\lambda)\| \|e(\lambda)\|} \right) \quad (3)$$

where λ is the wavelength range of reflectance spectra, $f(\lambda)$ is the image pixel spectra, and $e(\lambda)$ is the sediment sample spectra measured using ASD (Chang, 2003). Smaller values represent a higher degree of similarity between the two spectra of interest. The degree of spectral

similarity was separately calculated using SAM for the VNIR (400–1400 nm) and SWIR (2000–2400 nm) ranges, for which spectral parameters were calculated.

4.2.3. Similarity of spectral parameters between image and ground datasets

To statistically assess the degree of similarity of spectral parameters between the image and ground dataset, a one-way ANOVA was performed for 29 ground samples within a main stream and image pixels corresponding to the sampling points. The null hypothesis in the one-way ANOVA was that there exist no significant differences between the mean values of parameters calculated from the image

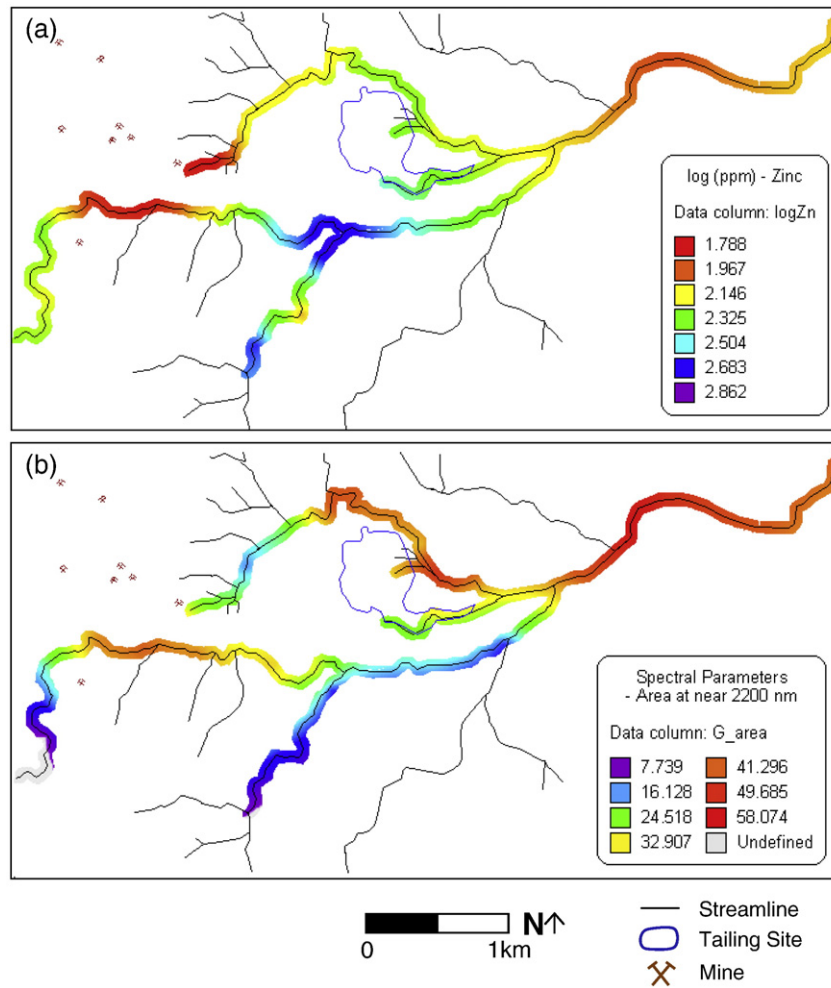


Fig. 4. Comparison of spatial patterns for gradient maps between (a) Zn concentration and (b) Area_{2200 nm} value.

and ground spectra. This null hypothesis was tested by calculating an *F*-value at a significance level of 0.05.

4.2.4. Classification of HyMAP image based on spectral parameters

Spectral parameters derived from ground data were applied to the classification of spectral responses related to heavy metals on HyMAP data. The parameters were calculated from the spectra of each image pixel after pre-processing (e.g., continuum-removal and normalization), and a rule image was produced for each parameter. A 40-m-wide bufferzone from the main streamline was considered as a study section, including 29 sampling points, to focus on the spread of pollution by stream water during the rainy season. The link between spectral parameters and heavy metal levels on the image was simplified via a binary fitness function (Legg et al., 2004; Debba et al., 2005). To obtain a map for screening heavy metals, the binary classes were characterized by whether the spectral response was significantly affected by heavy metals. A threshold for each parameter, S_t , for classification associated with heavy metal levels was defined by the spectral parameter value corresponding to a high concentration of heavy metal (i.e., exceeding the average concentration of each heavy metal). Each spectral parameter value, $S(x_{ij})$, was classified according to the following binary fitness function:

$$w_s(x_{ij}) = \begin{cases} 0, & \text{if } S(x_{ij}) < S_t \\ 1, & \text{if } S(x_{ij}) \geq S_t \end{cases} \quad (4)$$

where x_{ij} , $i=1,2,\dots, n$, and $j=1,2,\dots, m$ represent the pixel spectra associated with the spatial location, i and j , respectively.

5. Results and discussion

5.1. Relationship between spectral parameters and heavy metal concentrations

5.1.1. Heavy metal concentrations

Arsenic, Cu, Pb, and Zn were analyzed as an indicator of the environmental impact of mining activity in the Rodalquilar area. The concentrations of these heavy metals in sediment samples are summarized in Table 1. The concentrations of heavy metals in most samples exceed the effects range-low (ERL) value of sediment quality guidelines (SQGs)⁴ in Table 2. On average, Pb showed the highest concentration of the four elements, with the concentrations of Cu, Zn, and As being between 129 and 292 ppm at every stream section. The highest As concentration was observed along path-I and co-path-I.

The spatial distribution of heavy metals observed in the gradient maps revealed two main spatial trends. The descriptive statistics are summarized in Table 1 and the distributions of Pb, Zn, and As concentrations are displayed in Figs. 3, 4, and 5, respectively. Arsenic concentrations show a marked increase along the tributary downstream from the tailing site (co-path-II). Relatively high concentrations of Pb, Zn, and Cu are recorded in the southern part of the study area and along the tributary that flows through the tailings. Extremely

⁴ Sediment quality guidelines (SQGs) were proposed by the National Oceanic and Atmospheric Administration of the USA to estimate the possible toxicological significance of chemical concentrations in sediments (McCready et al., 2006).

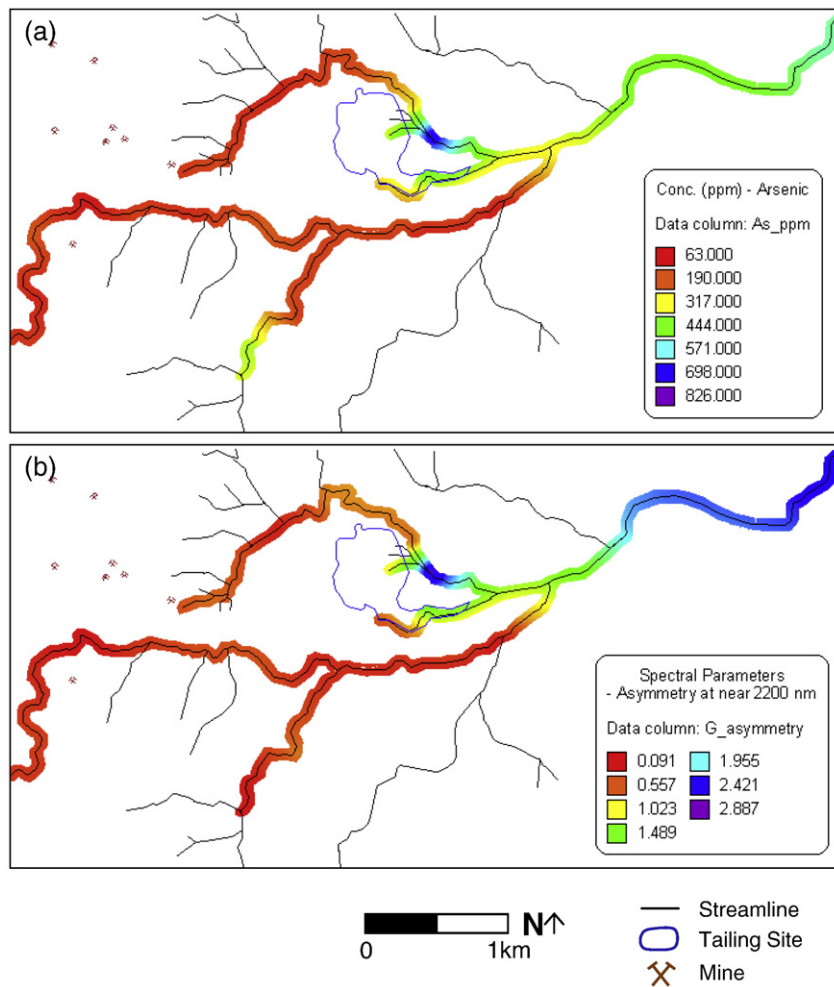


Fig. 5. Comparison of spatial patterns in gradient maps for (a) As concentration and (b) $Asym_{2200\text{ nm}}$.

high values of Pb are found along path-III, draining from an abandoned Pb–Zn mine, although the values show a marked decrease in downstream sections. Zn and Cu concentrations are slightly elevated along the upper part of the path-II streamline and the upper stream of path-I, where the stream passes through an abandoned gold-mining area, as well as those areas that record high Pb concentrations. Pb and Zn concentrations show slight increases in downstream areas.

5.1.2. Spectral parameters

As shown in Fig. 2, several variations in spectral absorption features show an association with heavy metal levels. In the visible range in association with FeO, band ratios between 610 and 500 nm ($n1/m1$) and between 1344 and 778 nm ($n2/m2$) were defined as a parameter caused by spectral variations (see Fig. 2(a)). In addition, the absorption peak depth, which is the distance from S to P at around

500 nm (see Fig. 2(b)), increases with high concentrations of heavy metals. The absorption depth and area values at around 2200 nm, where lattice OH in minerals is found, decrease with higher concentrations of heavy metals (Fig. 2(c)). These variations were defined as the spectral parameters, $Depth_{500\text{ nm}}$, $R_{610,500\text{ nm}}$, $R_{1344,778\text{ nm}}$, $Depth_{2200\text{ nm}}$, $Area_{2200\text{ nm}}$, and $Asym_{2200\text{ nm}}$, respectively.

5.1.3. Statistical correlation with geochemical values and spectral parameters

The strengths of the relationships between spectral parameters and heavy metal concentrations were defined using the Pearson correlation coefficient, as summarized in Table 3. Three spectral parameters, $R_{610,500\text{ nm}}$, $Area_{2200\text{ nm}}$, and $Asym_{2200\text{ nm}}$, showed a significant correlation with heavy metal concentrations on log scale. Copper showed weak correlations with all spectral parameters, and its relationship with $R_{610,500\text{ nm}}$ and $Area_{2200\text{ nm}}$ was statistically

Table 3

Pearson correlation coefficients between ground-derived spectral parameters and heavy metal concentrations on logarithmic scale

Element	$Depth_{500\text{ nm}}$	$R_{1344,778\text{ nm}}$	$R_{610,500\text{ nm}}$	$Depth_{2200\text{ nm}}$	$\log(Area_{2200\text{ nm}})$	$Asym_{2200\text{ nm}}$
log (Cu)	0.253	0.101	0.462**	-0.168	-0.447**	-0.195
log (Pb)	0.349*	0.126	0.708**	-0.247	-0.511**	-0.037
log (Zn)	0.538**	0.165	0.634**	-0.468**	-0.715**	-0.253
log (As)	-0.050	0.043	0.096	0.432**	0.466**	0.810**
log (Tot)	0.412**	0.142	0.748**	-0.332*	-0.614**	-0.152

* Correlation is significant at the 0.05 level.

** Correlation is significant at the 0.01 level.

Table 4

Statistical description of the performance of calibration models (stepwise and enter multiple linear regression) associated with heavy metal levels and ground-derived spectral parameters

Regression	Predictor	F	p-value	R ²	SEE ^a	RPD ^b	SDV ^c
<i>Stepwise multiple linear regression</i>							
log (Pb)	R _{610,500 nm}	38.341	0.000	0.530	0.382	1.362	0.520
log (Zn)	log (Area _{2200 nm})	30.169	0.000	0.470	0.243		
	log (Area _{2200 nm}), R _{610,500 nm}	5.528	0.025	0.546	0.228	1.395	0.318
log (As)	Asym _{2200 nm}	72.901	0.000	0.682	0.170		
	Asym _{2200 nm} , R _{610,500 nm}	21.607	0.000	0.808	0.134		
	log (Area _{2200 nm}), R _{610,500 nm} , Asym _{2200 nm}	7.082	0.012	0.843	0.123	2.386	0.293
	R _{610,500 nm}	49.500	0.000	0.593	0.288	1.456	0.419
<i>Enter multiple linear regression</i>							
log (Pb)	Depth _{500 nm} , R _{610,500 nm}	7.727	0.000	0.615	0.374	1.390	0.520
log (Zn)	R _{1344,778 nm} , Depth _{2200 nm}	7.132	0.000	0.596	0.230	1.387	0.318
log (As)	log (Area _{2200 nm}), R _{610,500 nm} , Asym _{2200 nm}	34.258	0.000	0.876	0.114	2.562	0.293
log (Tot)	Asym _{2200 nm}	8.965	0.000	0.650	0.289	1.447	0.419

^a Standard error of estimate.
^b Ratio of prediction deviation.
^c Standard deviation of validation set.

significant, with a *p*-value less than 0.01. Lead and total concentrations of heavy metals had the highest correlation coefficients: 0.71 and 0.75, respectively. These two geochemical values showed similar trends of

correlations with the analyzed parameters. In terms of Zn, Area_{2200 nm} showed the strongest relationship, with a correlation coefficient of -0.72. The negative sign of the correlation supports the hypothesis that if heavy metals combine to the surface functional group, e.g., ROH (Formulas 1 and 2), it is possible that the absorption feature of the group at the assigned spectral position might weaken because of a decrease in the amount of ROH at the mineral surface. Arsenic concentrations had a statistically significant correlation with Asym_{2200 nm} (*R*=0.81) at a significant level of 0.01.

5.1.4. Comparison of spatial distribution patterns

Based on the correlation results, the gradient maps of spectral parameters were compared with maps showing heavy metal concentrations on log scale in association with the distribution pattern along the studied streamline. R_{610,500 nm}, Area_{2200 nm}, and Asym_{2200 nm} showed similar spatial patterns to Pb and total concentrations, Zn, and As concentrations, respectively. In Fig. 3, the gradient maps of Pb and total concentrations show the same pattern, and the map associated with R_{610,500 nm} value shows a similar distribution pattern to both geochemical maps. In particular, these patterns show a good likeness in most sections of stream channels except for path-II. In the Area_{2200 nm} map (Fig. 4 (b)), the color legend was inverted due to the negative correlation with Zn concentrations. The Area_{2200 nm} and Zn maps display comparable patterns along path-III, co-path-I, and co-path-II, but values on the Area_{2200 nm} map are higher than those on the Zn map along path-I and the upper part of

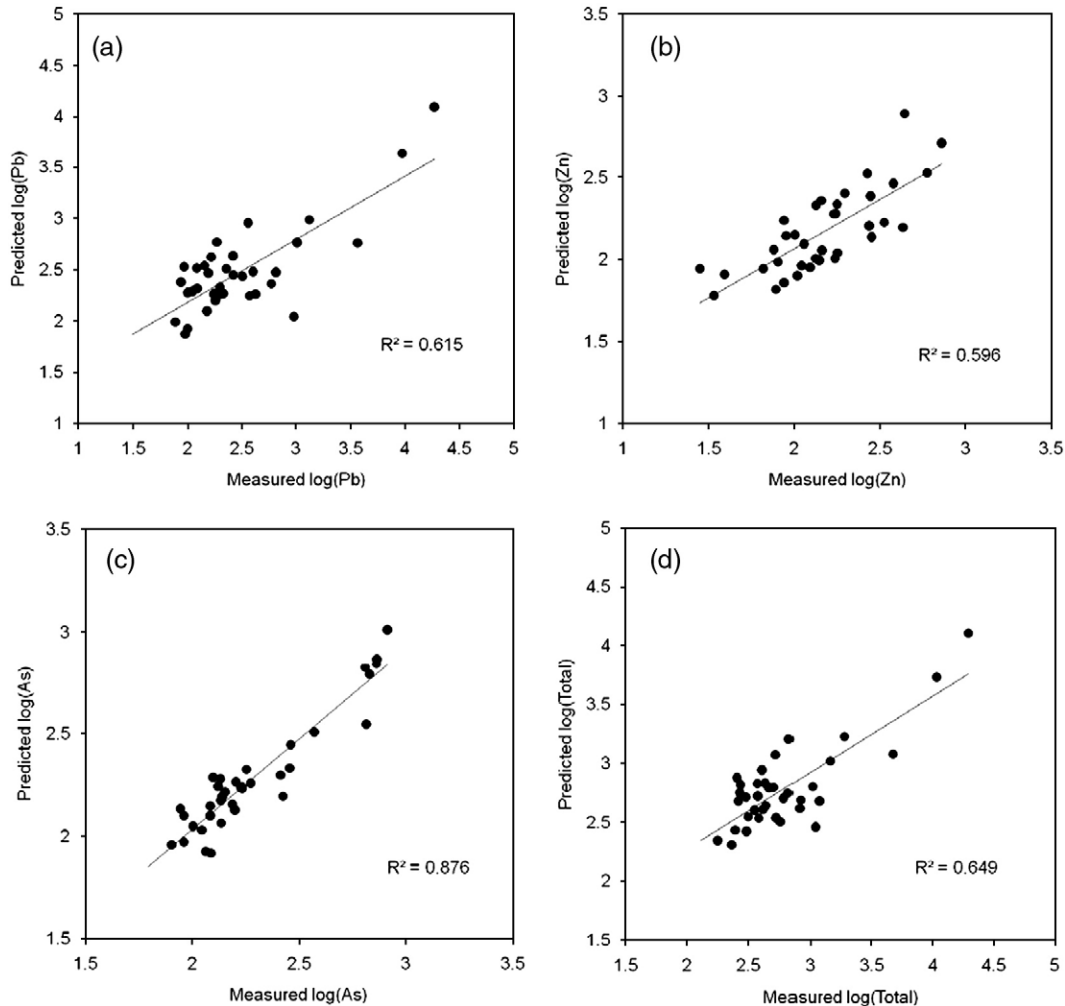


Fig. 6. Measured vs. predicted heavy metal concentrations plotted on a log scale, as derived from an enter multiple linear regression model using ground-derived spectral parameters. (a) Lead. (b) Zinc. (c) Arsenic. (d) Total concentrations.

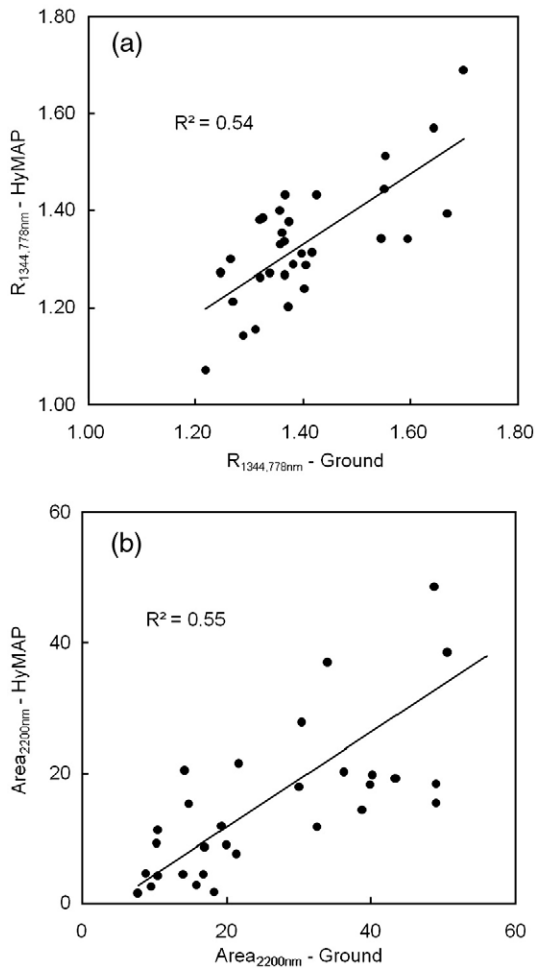


Fig. 7. Scatter plot of spectral parameter values, (a) $R_{1344,778\text{ nm}}$ and (b) $\text{Area}_{2200\text{ nm}}$, for classified HyMAP image pixels and ground spectrometer data.

path-II (Fig. 4). Overall, the pattern apparent in the $\text{Asym}_{2200\text{ nm}}$ map is comparable to that on the map showing the distribution of As concentration, although discrepancies are observed along the upper part of path-III (Fig. 5). The map of As concentrations on a log scale shows numerous differences in spatial pattern compared with the

Table 5
Results of one-way ANOVA between ground- and image-derived parameter values

Spectral parameter	ANOVA	Path-I	Path-II	Path-III and co-path-I	Co-path-II	Total
$\text{Depth}_{500\text{ nm}}$	<i>p</i> -value	0.006	0.730*	0.001	0.261*	0.001
	<i>F</i>	9.501	0.125	21.902	1.497	13.042
	F_{critical}	4.414	4.844	4.747	5.591	4.027
$R_{610,500\text{ nm}}$	<i>p</i> -value	0.000	0.030	0.061*	0.585*	0.000
	<i>F</i>	27.139	6.624	4.451	0.351	21.874
	F_{critical}	4.494	5.117	4.965	7.709	4.030
$R_{1344,778\text{ nm}}$	<i>p</i> -value	0.412*	0.830*	0.854*	0.626*	0.859*
	<i>F</i>	0.705	0.048	0.035	0.264	0.032
	F_{critical}	4.414	4.747	4.747	5.987	4.020
$\text{Depth}_{2200\text{ nm}}$	<i>p</i> -value	0.020	0.000	0.435*	0.001	0.000
	<i>F</i>	6.649	52.877	0.660	38.823	14.903
	F_{critical}	4.494	4.965	4.965	5.987	4.013
$\text{Area}_{2200\text{ nm}}$	<i>p</i> -value	0.123*	0.001	0.409*	0.000	0.001
	<i>F</i>	2.619	20.239	0.732	93.179	11.293
	F_{critical}	4.414	4.747	4.747	5.318	4.013
$\text{Asym}_{2200\text{ nm}}$	<i>p</i> -value	0.003	0.034	0.066*	0.001	0.001
	<i>F</i>	12.458	6.044	4.245	45.716	12.344
	F_{critical}	4.494	4.965	4.965	5.987	4.013

* No significant differences at $p > 0.05$.

$\text{Asym}_{2200\text{ nm}}$ map; consequently, the raw value of As concentration was used in producing a gradient map that showed a good likeness to the distribution pattern of the geochemical map.

5.1.5. Quantitative relationships

Quantitative relationships between metal concentrations and spectral parameters are listed in Table 4. Results are shown for all predictions with $R^2 > 0.5$. Two kinds of multiple linear regressions, stepwise and enter methods for selecting predictor variables, were applied. For stepwise linear regressions, $R_{610,500\text{ nm}}$, $\text{Area}_{2200\text{ nm}}$, and $\text{Asym}_{2200\text{ nm}}$ were mainly used as predictors. Of the parameters used for validation, $R^2 (> 0.5)$, RPD (> 1.3), and SEE (< 0.4) lay in reliable ranges. Prediction results for Zn using $R_{610,500\text{ nm}}$ and $\text{Area}_{2200\text{ nm}}$ and Pb and total value using $R_{610,500\text{ nm}}$ indicated a weak relationship ($R^2 > 0.5$). Prediction of As using $R_{610,500\text{ nm}}$, $\text{Area}_{2200\text{ nm}}$, and $\text{Asym}_{2200\text{ nm}}$ showed a more reliable result: $R^2 = 0.843$, RPD = 2.386, and SEE = 0.123. In terms of enter multiple linear regression, all six spectral parameters were included in the regression as a predictor. Their prediction performances for Pb, Zn, As, and total value was superior to those of the stepwise method. For the enter multiple linear model, predicted and measured heavy metal concentrations are compared in a scatter plot using a log scale (Fig. 6).

According to the prediction results of the linear regression model, ground-spectra-derived spectral parameters raise the possibility of a quantitative approach for heavy metal concentrations except for copper; in particular, multiple linear regression employing the enter method.

5.2. Application of the spectral parameters to a HyMAP image

5.2.1. Spectral similarity

The mean values obtained using SAM indicate a high degree of similarity ($\text{SAM} < 0.1$) between HyMAP image spectra and ground spectrometer spectra. SAM values for spectra in the SWIR range (2000–2500 nm) ($\text{SAM}_{\text{SWIR}} = 0.037$) are lower than those in the VNIR range (400–1200 nm) ($\text{SAM}_{\text{VNIR}} = 0.087$), meaning that the spectral parameters in the SWIR range in the HyMAP image might be more similar to the parameters derived from the ground spectra. These results indicate that spectral parameters derived from ground spectra could be applied to the image dataset in both wavelength ranges.

5.2.2. Comparison between ground- and image-derived spectral parameter

To assess the degree of similarity of obtained spectral parameter values between ground and images, the R^2 value and one-way ANOVA was calculated between ground spectrometer data and those image pixels that correspond to the field sampling sites. $R_{610,500\text{ nm}}$ and $\text{Area}_{2200\text{ nm}}$ in the scatter plot (Fig. 7) show weak relationships between the image and ground datasets for each of the 29 sampling points in the main stream ($R^2 > 0.5$), while the other parameters record R^2 values below 0.5.

In terms of the one-way ANOVA of populations for $\text{Depth}_{500\text{ nm}}$, $R_{610,500\text{ nm}}$, and $\text{Area}_{2200\text{ nm}}$, *p*-values were below 0.05 and *F*-values were larger than critical values, meaning that these parameters showed

Table 6
Statistics of spectral parameters calculated from ground data and image data

Spectral parameters	Ground			Image		
	Mean	Max	Min	Mean	Max	Min
$\text{Depth}_{500\text{ nm}}$	0.199	0.247	0.126	0.115	0.316	0.053
$R_{610,500\text{ nm}}$	1.892	2.049	1.801	1.676	1.791	1.519
$R_{1344,778\text{ nm}}$	1.325	1.418	1.148	1.356	1.492	1.240
$\text{Depth}_{2200\text{ nm}}$	0.559	0.727	0.293	0.350	0.829	0.040
$\text{Area}_{2200\text{ nm}}$	34.377	50.630	15.853	21.916	60.587	1.504
$\text{Asym}_{2200\text{ nm}}$	1.196	2.887	0.198	-0.037	1.259	-0.739

a significant difference between the image and ground datasets; however, we also calculated ANOVA within each stream section because the populations of these parameters recorded different mean values in each stream section (Table 5). The one-way ANOVA results for Depth_{500 nm} values along path-II and co-path-II indicated that the populations of the image and spectral parameters are statistically similar. For Area_{2200 nm}, path-I and path-III and co-path-I exhibit no significant difference between the two populations. In terms of R_{610,500 nm}, the two datasets showed similar populations along co-path-II and path-III and co-path-I. The *F*-value calculated for image and ground R_{1344,778 nm} data was smaller than the corresponding critical *F*-value (*p*=0.859); therefore, there are no significant differences in R_{1344,778 nm} values, and the ANOVA results for all stream sections also showed statistical similarity between the two datasets. Depth_{2200 nm}

and Asym_{2200 nm} showed significant differences in the population between image and ground, except for path-III and co-path-I.

The differences in spectral parameter values between image and ground data might be explained by the contrasting scales of observation. In terms of comparing spectrum values, spectrometer data for ground samples were fine-scaled, covering a single point, a spot size of 10 mm for the measurement, whereas each pixel on the HyMAP image contained the average reflectance of a 4×4 m surface area. Even though the pixel spectra on the classified image, corresponding to the GPS coordinates of the field sampling point, are similar to the spectrometer data, the spectral response could include differences between the image and spectrometer data due to the measurement scale. In addition, in comparing maps, the gradient map interpolating the parameter values derived from spectrometer

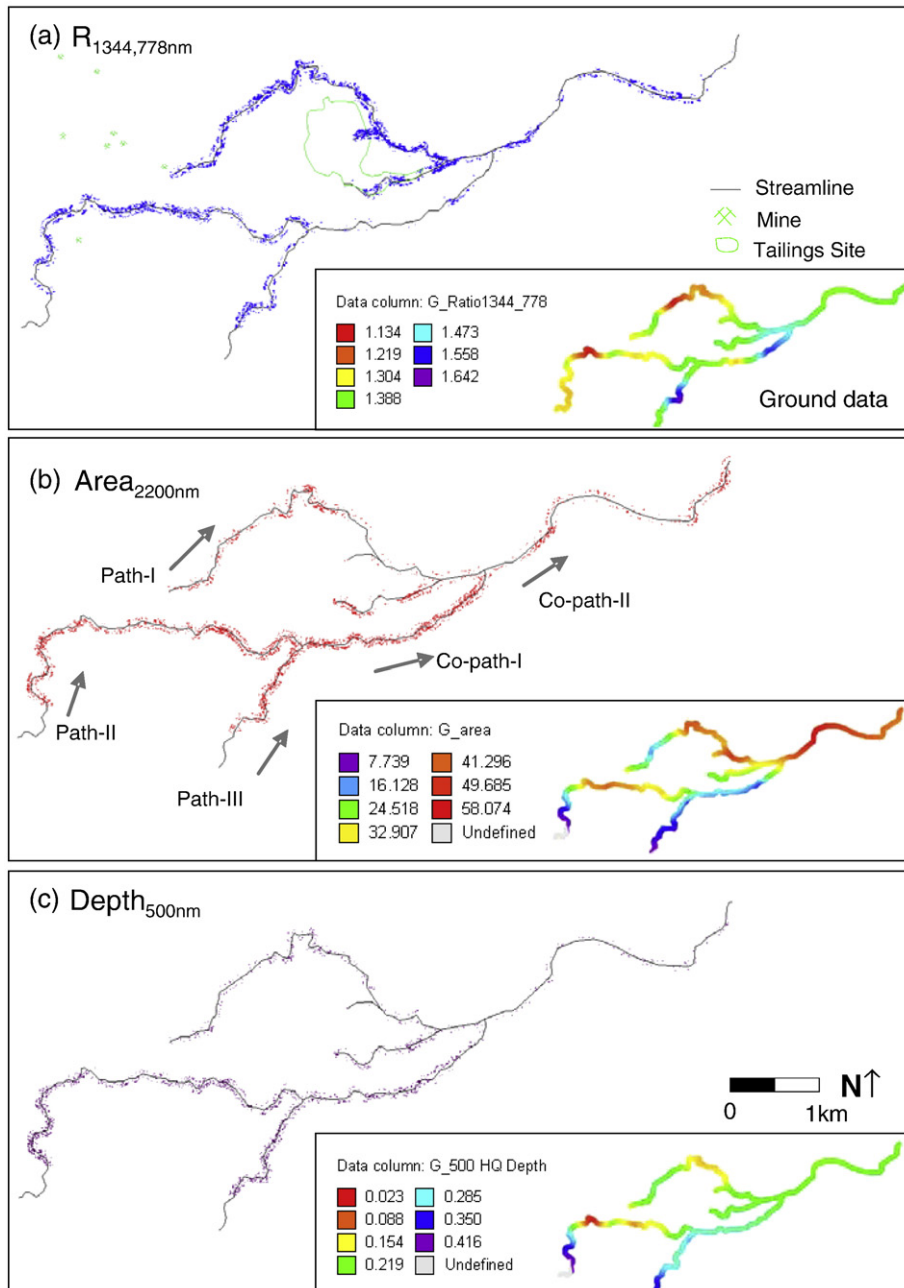


Fig. 8. Distribution maps of spectral parameter values, (a) R_{1344,778 nm}, (b) Area_{2200 nm}, and (c) Depth_{500 nm}, classified from HyMAP image pixels, comparing gradient maps for spectral parameters derived from ground data (inset figures).

data employed a coarse spatial resolution representing the sampling interval, downscaled for mapping.

5.2.3. Spatial distribution patterns of classified image pixels

The spectral parameters were calculated with HyMAP image pixels, and each parameter produced a rule image for extended observations from pixels of the sampling point to the area adjacent to the streamline. The parameter values for each stream section derived from the HyMAP image are compared with those from the ground dataset in Table 6. The rule images associated with spectral parameters were classified based on threshold values. Fig. 8 shows the classification results of the HyMAP image for spectral parameters. Of the six spectral parameter rule images, the distribution pattern of classified images for Depth_{500 nm}, R_{1344,778 nm}, and Area_{2200 nm} showed a similarity to the spatial patterns in the gradient map of the ground dataset. In particular, similar patterns were recorded along the upper part of path-III and the tributary flowing from the tailings site, corresponding to higher concentrations of heavy metals. The classified pixels indicate that the spectral parameter values shown on the map represent above-average heavy metal concentrations, according to the definition of the threshold value employed in the classification procedure.

In terms of R_{1344,778 nm}, image pixels along parts of path-I around the tailing dump and path-III were classified as having higher parameter values than those on the ground parameter map, and lower values were recorded along co-path-I (Fig. 8 (a)). For the Area_{2200 nm} map, the distribution pattern showed similar results for the two datasets in all areas except for the middle sections of path-I and path-II (Fig. 8 (b)). For the Depth_{500 nm} map, those sections with higher values recorded comparable patterns between the image and ground datasets, whereas image pixels showed relatively high values along the middle sections of path-I and path-II, which recorded relatively low values in the ground dataset (Fig. 8 (c)).

6. Conclusions

This study examined the possible use of spectral indicators obtained from a field sample in estimating heavy metals, as well as extending their use to image data in mapping heavy metal distributions as an initial step to retrieving heavy metals from image-derived spectral parameters and quantitatively mapping their distribution. Parameters derived from the spectra of sediment samples were linked to heavy metals and extended to HyMAP images. From variations in the spectral absorption features of ROH (R: Al, Si, Mn, Fe, etc.) and RO (i.e., FeO) at mineral surfaces, Depth_{500 nm}, R_{610,500 nm}, and R_{1344,778 nm} in the VNIR range and Depth_{2200 nm}, Area_{2200 nm}, and Asym_{2200 nm} in the SWIR range were derived as spectral parameters associated with heavy metals, based on the theory of metal binding reactions. The ground-derived spectral parameters R_{610,500 nm}, Asym_{2200 nm}, and Area_{2200 nm} showed statistically significant relationships with Pb, As, and Zn, respectively, as well as similar spatial patterns on the compiled maps. This result indicates that spectral parameter values are directly related to heavy metals, and can be used to screen them on a map. Moreover, the reliable nature of results obtained by multiple linear regressions (generally, R²>0.5, RPD>1.3, and SEE<0.4) between the ground-derived spectral parameters and heavy metal concentrations indicates the feasibility of retrieving heavy metal concentrations from spectral absorption feature parameters.

Based on ground measurements, spectral parameters were derived from a HyMAP image after assessing the degree of similarity of the spectra of HyMAP image pixels, corresponding to the sampling locations of ground data, with ground-measured spectra. Image-derived spectral parameters were compared with ground-spectra-derived parameters based on R², ANOVA, and spatial pattern. The R_{1344,778 nm} and Area_{2200 nm} parameters showed a weak relationship between the two datasets (R²>0.5). Populations of the image-derived

spectral parameter values Depth_{500 nm}, R_{1344,778 nm}, and Area_{2200 nm} were comparable with those of ground-derived spectral parameters along a section of the stream channel. Extending the observation from each pixel of the sampling points to the area adjacent to the streamline, the spatial pattern of classified pixels in the rule images of the Depth_{500 nm}, R_{1344,778 nm}, and Area_{2200 nm} parameters are somewhat similar to the spectral parameter distribution of sediment samples in the gradient map. Areas in the classified image that corresponded to higher values in the ground gradient map showed a closer match.

These results show that some of the spectral parameters derived from the spectra of sediment samples can be applied to the image dataset, although differences in observation scales between image (4×4 m resolution) and spectrometer data (spot point of 10 mm diameter) could lead to discrepancies in spectral parameter values between the ground and image datasets. As a further step, the retrieval of heavy metals and quantitative mapping using spectral parameters derived from hyperspectral images should take into account differences in the spectral and spatial resolution between ground spectrometer data and image data. Despite the requirement for further corrections, spectral absorption feature parameters considered in the present study showed the potential to detect heavy metals, and the image-derived spectral parameters themselves showed a capacity to screen areas affected by heavy metals as a preliminary observation in determining sampling strategies and precise analyses in investigating environmental pollution.

Acknowledgments

This work was supported by the Korea Science and Engineering Foundation (KOSEF) through the National Research Lab. program funded by the Korean Ministry of Science and Technology (No. M10300000298-06J0000-29810). The authors would like to thank the International Institute for Geo-information Science and Earth Observation (ITC) for their support in providing data and discussion during the research visit supported by the Korea Research Foundation Grant funded by the Korean Government (MOEHRD) (KRF-2006-612- D00053).

References

- Arribas, A., Jr., Rytuba, J. J., Rye, R. O., Cunningham, C. G., Podwysocki, M. H., Kelly, W. C., et al. (1989). Preliminary study of the ore deposits and hydrothermal alteration in the Rodalquilar Caldera Complex, southeastern Spain. *USGS open-file Report 89-327* (pp. 39). Reston, VA: U.S. Geological Survey.
- Ben-Dor, E., Irons, J. R., & Epema, G. F. (1999). Soil reflectance. In A. N. Rencz (Ed.), *Remote sensing for the earth sciences: Manual of remote sensing* (pp. 111–188). New York: John Wiley & Sons.
- Chang, Chein-I. (2003). *Hyperspectral imaging: Techniques for spectral detection and classification* (pp. 20–21). New York: Kluwer Academic.
- Christl, I., & Kretzschmar, R. (1999). Competitive sorption of copper and lead at the oxide–water interface: Implication for surface site density. *Geochimica et Cosmochimica Acta*, 63(19/20), 2929–2938.
- Clark, R. N., & Roush, T. L. (1984). Reflectance spectroscopy: Quantitative analysis techniques for remote sensing applications. *Journal of Geophysical Research*, 89(B7), 6329–6340.
- Cocks, T., Janssens, R., Stewart, W. I., & Shields, T. (1998). The HYMAP airborne hyperspectral sensor: The system, calibration and performance. *First EARSel workshop on imaging spectroscopy*: Zurich.
- Debba, P., van Ruitenbeek, F. J. A., van der Meer, F. D., Carranza, E. J. M., & Stein, A. (2005). Optimal field sampling for targeting minerals using hyperspectral data. *Remote Sensing of Environment*, 99, 373–386.
- Dzombak, D. A., & Morel, F. M. M. (1990). *Surface complexation modeling: Hydrous ferric oxides* (pp. 9–42). New York: Wiley.
- Farrand, W. H., & Harsanyi, J. C. (1997). Mapping the distribution of mine tailings in the Coeur d'Alene River Valley, Idaho, through the use of a constrained energy minimization technique. *Remote Sensing of Environment*, 59, 64–76.
- Ferrier, G. (1999). Application of imaging spectrometer data in identifying environmental pollution caused by mining at Rodalquilar, Spain. *Remote Sensing of Environment*, 68, 125–137.
- Gaffey, S. J., McFadden, L. A., Nash, D. I., & Pieters, C. M. (1993). Ultraviolet, visible, and near-infrared reflectance spectroscopy: Laboratory spectra of geology materials. In C. M. Pieters, & P. A. J. Englert (Eds.), *Remote geochemical analysis: Elemental and mineralogical composition* (pp. 43–77): Cambridge University Press.

- Hartman, J. (2000). *An interactive tutorial for SPSS 10.0 for Windows: Multiple linear regression*.
- Kemper, T., & Sommer, S. (2002). Estimate of heavy metal contamination in soils after a mining accident using reflectance spectroscopy. *Environmental Science and Technology*, 36, 2742–2747.
- Kruse, F. A., Lefkoff, A. B., Boardman, J. B., Heidebrecht, K. B., Shapiro, A. T., Barloon, P. J., et al. (1993). The Spectral Image Processing System (SIPS)—Interactive visualization and analysis of imaging spectrometer data. *Remote Sensing of Environment*, 44, 145–163.
- Legg, S., Hutter, M., & Kumar, A. (2004). Tournament versus fitness uniform selection. *Technical Report IDSIA-04-04 of IDSIA: Istituto Dalle Molle di Studi sull'Intelligenza Artificiale*.
- McCready, S., Birch, G. F., & Long, E. R. (2006). Metallic and organic contaminants in sediments of Sydney Harbour, Australia and vicinity—A chemical dataset for evaluating sediment quality guidelines. *Environment International*, 32(4), 455–465.
- Montero, S., I.C., Brimhall, G. H., Alpers, C. N., & Swayze, G. A. (2005). Characterization of waste rock associated with acid drainage at the Penn Mine, California, by ground-based visible to short-wave infrared reflectance spectroscopy assisted by digital mapping. *Chemical Geology*, 215(1–4 SPEC. ISS.), 453–472.
- Moreno, T., Oldroyd, A., McDonald, I., & Gibbons, W. (2007). Preferential fractionation of trace metals-metalloids into PM10 resuspended from contaminated gold mine tailings at Rodalquilar, Spain. *Water, Air And Soil Pollution*, 179(1–4), 93–105.
- Roberts, D., Nachttegaal, M., & Sparks, D. L. (2005). Speciation of metals in soils. In M. A. Tabatabai, & D. L. Sparks (Eds.), *Chemical processes in soils* (pp. 619–654). Wisconsin: Soil Science Society of America.
- Rytuba, J. J., Arribas, A., Jr., Cunningham, C. G., McKee, E. H., Podwysocki, M. H., Smith, J. G., et al. (1990). Mineralized and unmineralized calderas in Spain; Part II, evolution of the Rodalquilar caldera complex and associated gold–alunite deposits. *Mineralium Deposita*, 25(1), S29–S35.
- Sares, M. A., Hauff, P. L., Peters, D. C., Coulter, D. W., Bird, D. A., Henderson, F. B., III, et al. (2004). Characterizing sources of acid rock drainage and resulting water quality impact using hyperspectral remote sensing—Examples from the upper Arkansas river basin, Colorado. *Advanced integration of geospatial technologies in mining reclamation, Dec. 7–9, 2004, Atlanta, GA*.
- Sparks, D. L. (1995). *Environmental soil chemistry* (pp. 99–139). San Diego: Academic Press.
- van der Meer, F. (2006). Indicator kriging applied to absorption band analysis in hyperspectral imagery: A case study from the Rodalquilar epithermal gold mining area, SE Spain. *International Journal of Earth Observation and Geoinformation*, 8, 61–72.
- Wray, D. S. (1998). The impact of unconfined mine tailings and anthropogenic pollution on a semi-arid environment—An initial study of the Rodalquilar mining district, south east Spain. *Environmental Geochemistry and Health*, 20, 29–38.
- Wu, Y. Z., Chen, J., Ji, J. F., Tian, Q. J., & Wu, X. M. (2005). Feasibility of reflectance spectroscopy for the assessment of soil mercury contamination. *Environmental Science and Technology*, 39(3), 873–878.
- Zachara, J. M., & Westall, J. C. (1999). Chemical modeling of ion adsorption in soils. In D. L. Sparks (Ed.), *Soil physical chemistry* (pp. 47–95). Boca Raton: CRC Press.